



Article

# Investigation of the Magnetic Circuit and Performance of Less-Rare-Earth Interior Permanent-Magnet Synchronous Machines Used for Electric Vehicles

Ping Zheng <sup>1,2</sup>, Weinan Wang <sup>1</sup> , Mingqiao Wang <sup>1</sup> , Yong Liu <sup>1,\*</sup> and Zhenxing Fu <sup>1</sup>

<sup>1</sup> Department of Electrical Engineering, Harbin Institute of Technology, Harbin 150080, China; zhengping@hit.edu.cn (P.Z.); wangweinan19900501@163.com (W.W.); 18846186348@163.com (M.W.); fuzhenxing@letv.com (Z.F.)

<sup>2</sup> State Key Laboratory of Robotics and System, Harbin Institute of Technology, Harbin 150080, China

\* Correspondence: yliu@hit.edu.cn; Tel.: +86-451-8641-3623

Received: 21 November 2017; Accepted: 11 December 2017; Published: 19 December 2017

**Abstract:** The less-rare-earth interior permanent-magnet synchronous machines (LRE-IPMSMs), which have the advantages of high power density, high efficiency, and low cost, are promising candidates for electric vehicles (EVs). In this paper, the equivalent magnetic circuit (EMC) of LRE-IPMSM is established and analyzed to investigate the machine design principles, and then the performance of an optimized machine is analyzed. Firstly, the equivalent magnetic circuits of the LRE-IPMSM are established by taking the saturation effect into consideration. Secondly, the effects of geometric parameters, such as the permanent-magnet (PM) width, the PM thickness, the flux barrier thickness, the flux barrier span angle, and the bridge width, on no-load flux,  $q$ -axis flux, and  $d$ -axis flux are investigated, respectively. The results calculated by the EMC method and finite-element analysis (FEA) are analyzed and compared, which proves the effectiveness of the EMC method. Finally, an optimized design of LRE-IPMSM obtained by the magnetic circuit analyses is proposed. The electromagnetic performances and mechanical strength of the optimized LRE-IPMSM are analyzed and verified, respectively.

**Keywords:** less rare earth; interior permanent-magnet synchronous machines; equivalent magnetic circuit (EMC); electromagnetic performance; mechanical strength

## 1. Introduction

Electric vehicles (EVs) have been extensively promoted in recent years as the energy shortage and environmental pollution become more and more serious [1,2]. Electric machines, which are the core component of EVs' driving system, have a significant impact on the performance of EVs. The requirements of electric machines used in EVs include high efficiency, high power density, and high power factor, etc. Rare-earth permanent-magnet synchronous machines (RE-PMMSMs) can meet all the above requirements. Hence, they are widely used in EVs as the traction motors [3,4].

However, in recent years, the dramatic price fluctuations of rare-earth permanent-magnets (PMs) have intensified efforts to seek alternative solutions [5]. One alternative is less-rare-earth interior permanent-magnet synchronous machines (LRE-IPMSMs), which make use of more reluctance torque and reduce the consumption of rare-earth materials. The LRE-IPMSMs adopt the rotor structure of multilayer flux barriers to obtain a high saliency ratio and improve the machine performance by inserting proper rare-earth PMs into flux barriers [6–9]. Hence, the arrangements of flux barriers and PMs are crucial to the LRE-IPMSMs. In [10], an analytical method is proposed, which concentrates on selecting the combinations of flux barrier shapes to reduce the torque harmonic. The torque

characteristics of the LRE-IPMSMs are improved by shifting the flux barrier location in [11]. Besides, the shapes of flux barriers also affect the demagnetization rate of the PMs. In [12], the rotor structure with tapered flux barriers is adopted to resist the PMs irreversible demagnetization. Although the rare-earth PMs inserted into the LRE-IPMSMs can obviously improve the torque density and power factor, the consumption should be controlled because of its high price. In [13], the influence of permanent-magnet (PM) quantity on the LRE-IPMSM performance is investigated and the minimization of PMs is obtained on the premise of taking the machine performance into consideration. An analytical method is proposed in [14], which focuses on the reduction of the PM quantity without affecting the torque performance. In [15], the performances of LRE-IPMSMs with various magnetic pole structures are analyzed and compared.

The equivalent magnetic circuit (EMC) method is practical and precise to study the machine. In [16,17], the no-load and demagnetization magnetic circuits of the LRE-IPMSMs are established to investigate machine performance. However, the influences of geometric parameters on magnetic circuits still need to be studied in detail. Besides, as the reluctance torque accounts for most of the electromagnetic torque in LRE-IPMSMs, the  $q$ -axis and  $d$ -axis magnetic circuits should be studied in that the reluctance torque is proportional to the difference between the  $q$ -axis flux and  $d$ -axis flux.

In this paper, the magnetic circuits of the investigated LRE-IPMSM are established to calculate and analyze the no-load flux,  $q$ -axis flux, and  $d$ -axis flux. Furthermore, the effects of geometric parameters on the no-load flux,  $q$ -axis flux, and  $d$ -axis flux are investigated. After that, an optimized design of LRE-IPMSM obtained by the magnetic circuit analyses is proposed. Finally, the electromagnetic performances of the optimized LRE-IPMSM are analyzed and the stress distribution of the optimized LRE-IPMSM is investigated to ensure the machine mechanical safety.

## 2. No-Load Magnetic Circuit Analysis

The electromagnetic torque ( $T_{EM}$ ) of LRE-IPMSMs consists of reluctance torque ( $T_{REL}$ ) and PM torque ( $T_{PM}$ ).  $T_{REL}$  is generated by the rotor saliency.  $T_{PM}$  is generated by the interaction of magnetic fields produced by the stator current and PMs.  $T_{EM}$  can be expressed as:

$$T_{EM} = T_{PM} + T_{REL} = p\psi_f i_d + p(\Psi_q i_d - \Psi_d i_q) \quad (1)$$

where  $p$  represents the pole pairs;  $\Psi_f$  is the no-load flux linkage;  $\Psi_q$  and  $\Psi_d$  are the  $q$ -axis and  $d$ -axis flux linkages, respectively; and  $i_q$  and  $i_d$  are the  $q$ -axis and  $d$ -axis currents, respectively.

From Equation (1), it can be found that the reluctance torque has a direct relationship with  $q$ -axis and  $d$ -axis fluxes. The PM torque also has a direct relationship with the no-load flux. Hence, it is significant to analyze the no-load,  $q$ -axis, and  $d$ -axis fluxes of the LRE-IPMSMs. Additionally, the accurate values of the no-load,  $q$ -axis, and  $d$ -axis fluxes are crucial to calculate the PM torque and reluctance torque precisely. The structure of the preliminary LRE-IPMSM is shown in Figure 1a. The sketches of flux barriers and bridges are shown in Figure 1b. As  $T_{REL}$  accounts for most of the  $T_{EM}$  in LRE-IPMSMs, the  $q$ -axis and  $d$ -axis in LRE-IPMSMs are defined to be the same as the reluctance machine, namely, the  $q$ -axis is aligned with the center of PMs and the  $d$ -axis is orthogonal with the  $q$ -axis in electrical degree. The basic parameters of the preliminary LRE-IPMSM are shown in Table 1.

### 2.1. No-Load Magnetic Circuit Model

The bridges, as shown in Figure 1b, are normally narrow to decrease the no-load leakage flux. This results in the saturation of the bridges in the no-load magnetic circuit. The magnetization curve of silicon steel is an approximate straight line in the saturation area, as shown in Figure 2. Hence the saturation area can be equivalent to a magnetomotive force (MMF) ( $F_{sa}$ ) and a serial-connected reluctance ( $R_{sa}$ ) [14].  $F_{sa}$  and  $R_{sa}$  are expressed as:

$$F_{sa} = \frac{B_{sa}}{\mu_{sa}\mu_0} \cdot h_{sa} \quad (2)$$

$$R_{Sa} = \frac{h_{Sa}}{\mu_{Sa}\mu_0 b_{Sa}L} \quad (3)$$

where  $\mu_0$  is the permeability of air and  $L$  is the lamination stack length.  $b_{sa}$  and  $h_{sa}$  are the width and length of the saturation area, respectively.  $B_{Sa}$  and  $\mu_{Sa}$  can be calculated by the magnetization curve of silicon steel, as shown in Figure 2.

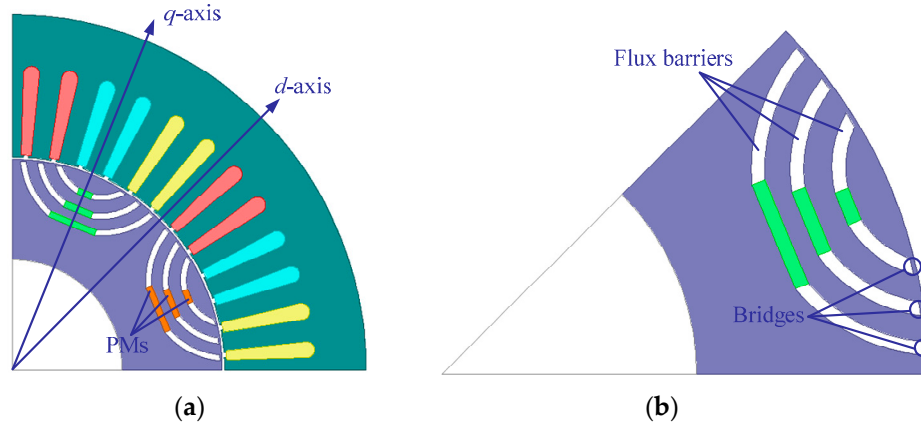


**Figure 1.** (a) Structure of the preliminary less-rare-earth interior permanent-magnet synchronous machine (LRE-IPMSM); (b) Sketches of flux barriers and bridges.

**Table 1.** Basic parameters of the preliminary less-rare-earth interior permanent-magnet synchronous machine (LRE-IPMSM).

Parameters	Unit	Value
Stator outer diameter	mm	290
Rotor outer diameter	mm	172
Air gap length	mm	1
Stack length	mm	106
Maximum speed	rpm	7000
Maximum torque	Nm	344
Maximum efficiency	%	96

The no-load EMC model of the investigated LRE-IPMSM is shown in Figure 3 and it is rewritten in Figure 4. The following equations can be obtained according to Kirchhoff's law:

$$\begin{cases} (R_{g_{\delta 1}} + R_{\delta 1})\Phi_{\delta 1} - R_{g_{\delta 2}}\Phi_{\delta 2} - F_{\delta 1} = 0 \\ R_{g_{\delta 2}}\Phi_{\delta 2} + R_{\delta 2}(\Phi_{\delta 1} + \Phi_{\delta 2}) - R_{g_{\delta 3}}\Phi_{\delta 3} - F_{\delta 2} = 0 \\ R_{g_{\delta 3}}\Phi_{\delta 3} + R_{\delta 3}(\Phi_{\delta 1} + \Phi_{\delta 2} + \Phi_{\delta 3}) - F_{\delta 3} = 0 \\ \Phi_{\delta} = \Phi_{\delta 1} + \Phi_{\delta 2} + \Phi_{\delta 3} \end{cases} \quad (4)$$

$$F_{\delta i} = \left( \frac{F_{PMi}}{R_{PMi}} - \frac{F_{Br_{\delta i}}}{R_{Br_{\delta i}}} \right) R_{\delta i} \quad (5)$$

$$\frac{1}{R_{\delta i}} = \frac{1}{R_{PMi}} + \frac{1}{R_{Ba_{\delta i}}} + \frac{1}{R_{Br_{\delta i}}} \quad (6)$$

where  $R_{g_{\delta i}}$  and  $R_{Ba_{\delta i}}$  are the air gap reluctance and flux barrier reluctance in the no-load magnetic circuit, respectively.  $F_{PMi}$  and  $R_{PMi}$  are the equivalent MMF and reluctance of PM, respectively.  $\Phi_{\delta i}$  is the segmental no-load flux that flows through  $R_{g_{\delta i}}$ , as shown in Figure 4.  $F_{\delta i}$  and  $R_{\delta i}$  are the equivalent MMF and reluctance of the corresponding flux barrier, PM, and bridge parallel circuit, respectively, as shown in Figure 5.

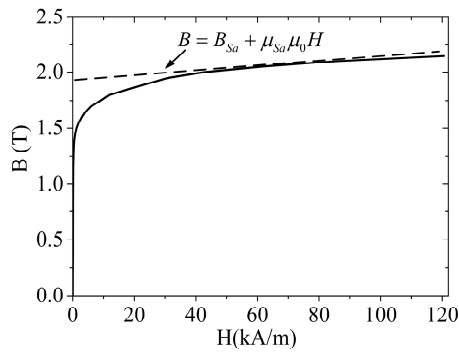


Figure 2. Magnetization curve of silicon steel.

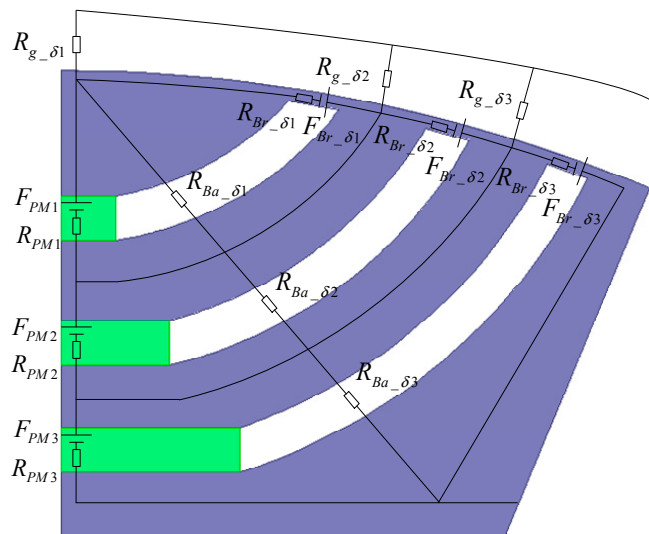


Figure 3. No-load magnetic circuit model.

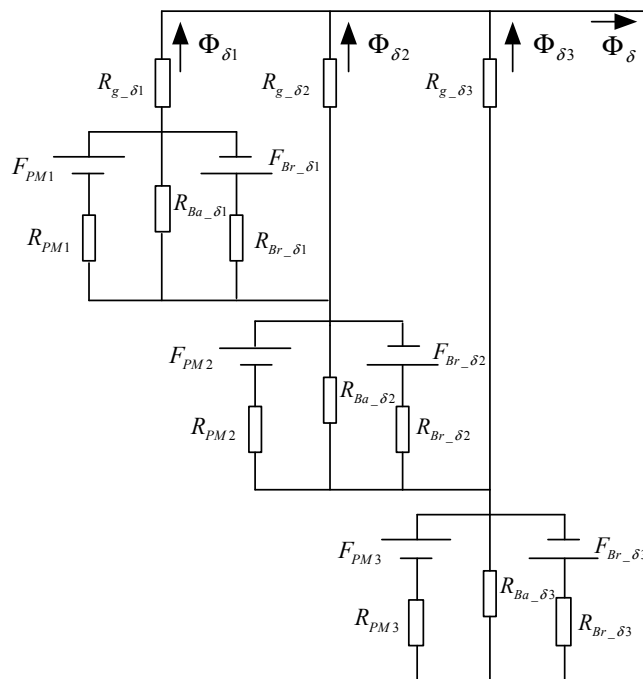


Figure 4. Rewriting of the no-load magnetic circuit model.

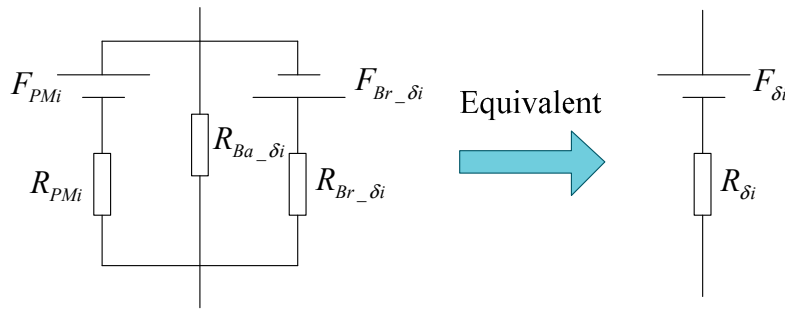


Figure 5. Equivalent of the flux barrier, permanent-magnet (PM) and bridge parallel circuit.

Therefore, the no-load flux ( $\Phi_\delta$ ) can be expressed as:

$$\Phi_\delta = \frac{F_{\delta 1} R_{g_\delta 2} R_{g_\delta 3} + F_{\delta 2} (R_{g_\delta 1} R_{g_\delta 3} + R_{\delta 1} R_{g_\delta 3} + R_{g_\delta 2} R_{g_\delta 3}) + F_{\delta 3} R_x}{(R_{g_\delta 1} + R_{\delta 1})(R_{g_\delta 2} + R_{\delta 2})(R_{g_\delta 3} + R_{\delta 3}) + R_{g_\delta 2} R_{g_\delta 3} R_{\delta 3} + (R_{g_\delta 1} + R_{\delta 1}) R_{g_\delta 3} R_{\delta 3} + (R_{g_\delta 3} + R_{\delta 3}) R_{g_\delta 2} R_{\delta 2}} \quad (7)$$

$$R_x = R_{g_\delta 1} R_{g_\delta 3} + R_{\delta 1} R_{g_\delta 3} + R_{g_\delta 1} R_{g_\delta 2} + R_{\delta 1} R_{g_\delta 2} + R_{g_\delta 1} R_{\delta 2} + R_{\delta 1} R_{\delta 2} + R_{g_\delta 2} R_{\delta 2} + R_{g_\delta 2} R_{g_\delta 3} \quad (8)$$

### 2.2. Geometric Parameters of the LRE-IPMSM

To study the design principle of LRE-IPMSMs, the effects of geometric parameters on the no-load flux,  $q$ -axis flux, and  $d$ -axis flux are investigated, respectively. The sketches of geometric parameters including the flux barrier span angle ( $\theta_{Bai}$ ), the flux barrier thickness ( $h_{Bai}$ ), the PM thickness ( $h_{PMi}$ ), the PM width ( $b_{PMi}$ ), and the bridge width ( $b_{Br}$ ) are shown in Figure 6a,b, respectively.

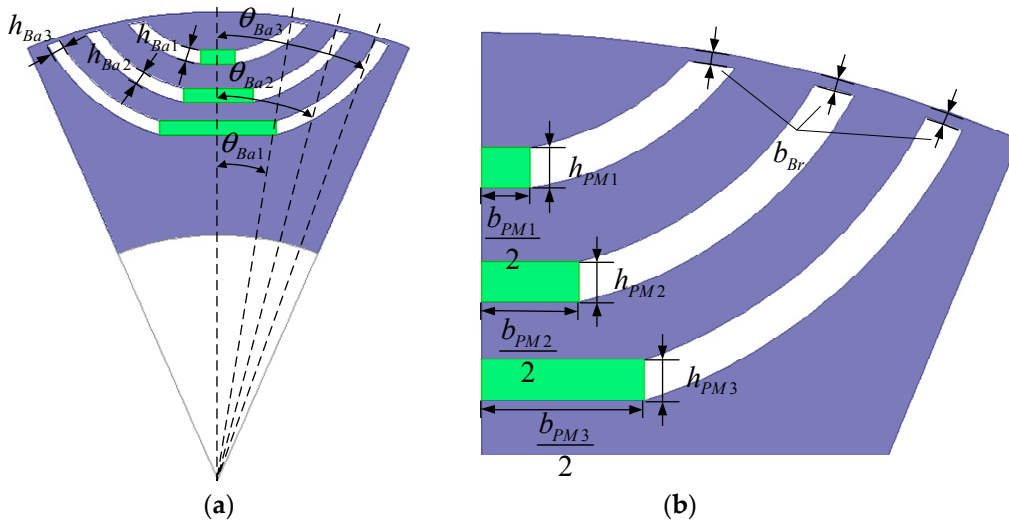
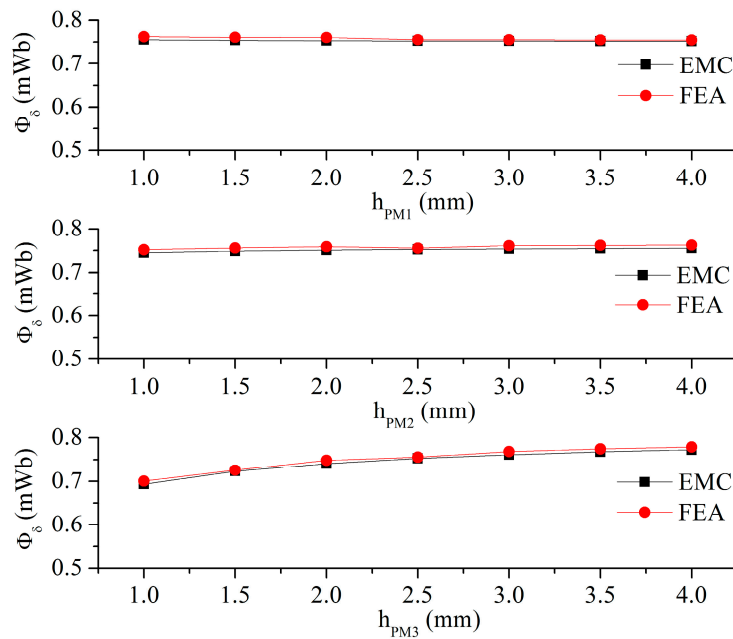


Figure 6. Sketches of geometric parameters: (a) the flux barrier span angle ( $\theta_{Bai}$ ) and the flux barrier thickness ( $h_{Bai}$ ); (b) the PM thickness ( $h_{PMi}$ ), the PM width ( $b_{PMi}$ ), and the bridge width ( $b_{Br}$ ).

### 2.3. Effect of PM Thickness on No-Load Flux

As mentioned before, a narrow bridge is adopted to decrease the no-load leakage flux. Therefore, the bridges are neglected (i.e.,  $b_{Br} = 0$ ) when the effects of geometric parameters (including  $h_{PMi}$ ,  $b_{PMi}$ ,  $h_{Bai}$ , and  $\theta_{Bai}$ ) on  $\Phi_\delta$  are investigated to analyze the no-load magnetic circuit conveniently. The effect of the bridge width on  $\Phi_\delta$  is analyzed in the following subsection.

The variation of  $\Phi_\delta$  with respect to the PM thickness ( $h_{PMi}$ ) is calculated by the EMC method and finite-element analysis (FEA), as shown in Figure 7. It can be seen that  $\Phi_\delta$  has a negligible variation with the increment of  $h_{PM1}$  and  $h_{PM2}$ , but  $\Phi_\delta$  increases slightly when  $h_{PM3}$  increases. This is because the coefficient of  $F_{\delta 3}$  is obviously larger than that of  $F_{\delta 1}$  and  $F_{\delta 2}$  in Equation (7).



**Figure 7.** No-load flux ( $\Phi_\delta$ ) versus the PM thickness ( $h_{PMi}$ ). EMC: equivalent magnetic circuit. FEA: finite-element analysis.

2.4. Effect of PM Width on No-Load Flux

The variation of  $\Phi_\delta$  versus the PM width ( $b_{PMi}$ ) is shown in Figure 8. To analyze the effect of  $b_{PMi}$  on  $\Phi_\delta$  simply, the flux barrier thickness is adjusted slightly to keep the reluctance of the flux barrier constant when  $b_{PMi}$  changes. It can be seen that  $\Phi_\delta$  increases linearly with the increment of  $b_{PMi}$ . This is because the flux produced by the PM is proportional to the PM width. By comparing Figures 7 and 8, it can be found that widening the PM to increase  $\Phi_\delta$  is more practical than thickening the PM. However, the design of PM thickness should take the irreversible demagnetization of the PM into consideration.

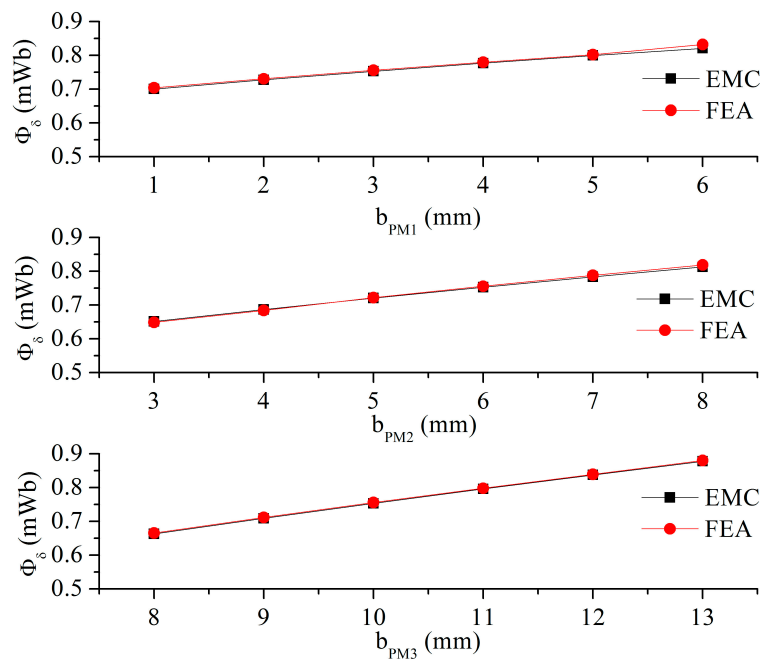


**Figure 8.** No-load flux ( $\Phi_\delta$ ) versus the PM width ( $b_{PMi}$ ).

### 2.5. Effect of Flux Barrier Thickness on No-Load Flux

The equivalent reluctance of the flux barrier can be expressed as:

$$R_{Ba\_i} = \frac{h_{Bai}}{\mu_0 b_{Bai} L} \quad (9)$$

where  $b_{Bai}$  is the flux barrier width.

According to the no-load magnetic circuit model and Equation (9), it can be found that changing the flux barrier width and thickness has the same effect on  $\Phi_\delta$  because they only change the equivalent reluctance of the flux barrier in the no-load magnetic circuit model. Hence, this paper only analyzes the effect of the flux barrier thickness on  $\Phi_\delta$  because the changing of the flux barrier thickness is more convenient than that of the flux barrier length.

The variation of  $\Phi_\delta$  with respect to the flux barrier thickness is shown in Figure 9. According to the analysis of the no-load magnetic circuit model, it can be known that the no-load fluxes flowing through  $R_{Ba\_i1}$  and  $R_{Ba\_i2}$  are ignorable. Hence the  $h_{Ba1}$  and  $h_{Ba2}$  have negligible impacts on  $\Phi_\delta$ , as seen in Figure 9. The flux, which flows through  $R_{Ba\_i3}$ , becomes the leakage flux instead of flowing through the air gap. Therefore, when  $h_{Ba3}$  increases, the leakage flux that flows through  $R_{Ba\_i3}$  decreases and  $\Phi_\delta$  increases, as shown in Figure 9.

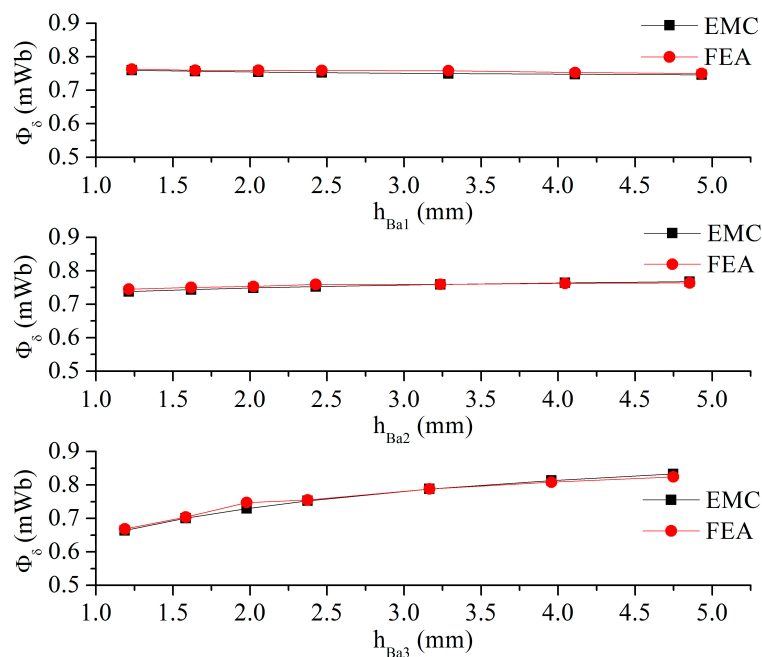
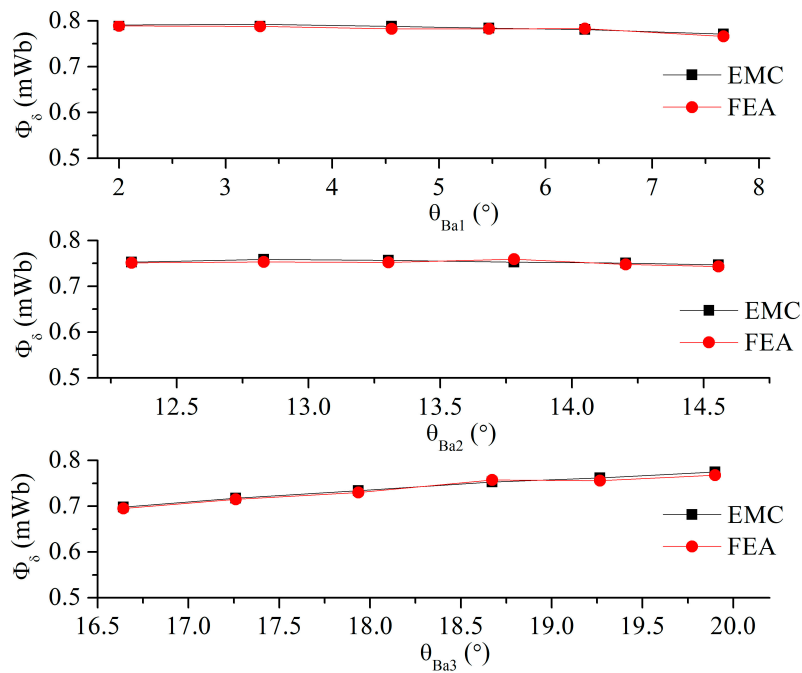


Figure 9. No-load flux ( $\Phi_\delta$ ) versus the flux barrier thickness ( $h_{Bai}$ ).

### 2.6. Effect of Flux Barrier Span Angle on No-Load Flux

Figure 10 shows the variation of  $\Phi_\delta$  with respect to the flux barrier span angle ( $\theta_{Bai}$ ). According to the no-load magnetic circuit model, it can be seen that  $R_{g\_i1}$  decreases and  $R_{g\_i2}$  increases with the increment of  $\theta_{Ba1}$ . Similarly,  $R_{g\_i2}$  decreases and  $R_{g\_i3}$  increases with the increment of  $\theta_{Ba2}$ . This results in the inconsiderable variation of  $\Phi_\delta$  when  $\theta_{Ba1}$  and  $\theta_{Ba2}$  vary, as shown in Figure 10. But when  $\theta_{Ba3}$  increases,  $R_{g\_i3}$  decreases, and  $R_{g\_i1}$ , as well as  $R_{g\_i2}$ , is invariable. Hence  $\Phi_\delta$  increases with the increment of  $\theta_{Ba3}$ , as shown in Figure 10.



**Figure 10.** No-load flux ( $\Phi_{\delta}$ ) versus the flux barrier span angle ( $\theta_{Ba1}$ ).

### 2.7. Effect of Bridge Width on No-Load Flux

Figure 11 shows the effect of the bridge width ( $b_{Br}$ ) on  $\Phi_{\delta}$ . As can be seen, when  $b_{Br}$  increases,  $\Phi_{\delta}$  decreases because the leakage flux that flows through the bridges increases. In other words, a narrow bridge is conducive to enhance  $\Phi_{\delta}$  but it may cause rotor fracture failure at the same time. Hence, the selection of  $b_{Br}$  should take the electromagnetic performance and mechanical safety into consideration simultaneously. The saturation level declines when the bridge width increases, which is not taken into consideration in the EMC method (i.e., the bridges are always considered to be saturated when  $b_{Br}$  increases). That leads to an increasing error between the results of the EMC method and FEA with the increment of  $b_{Br}$ , as shown in Figure 11.

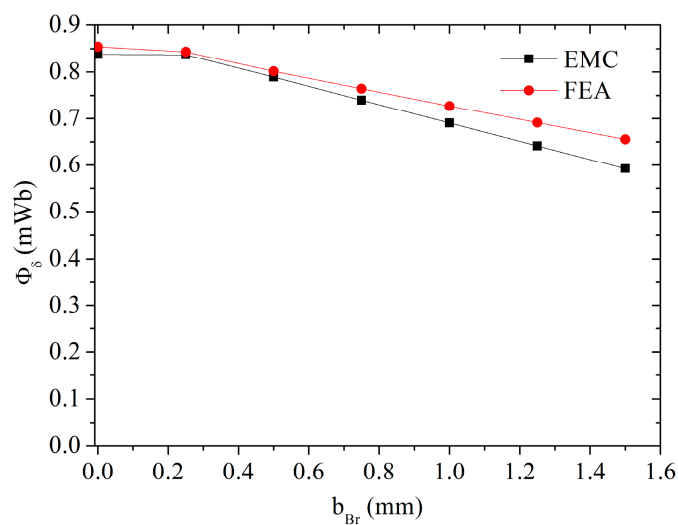


**Figure 11.** No-load flux ( $\Phi_{\delta}$ ) versus the bridge width ( $b_{Br}$ ).



### 3. *q*-Axis Magnetic Circuit Analysis

#### 3.1. *q*-Axis Magnetic Circuit Model

The PMs are removed in the analyses of the *q*-axis and *d*-axis magnetic circuits. The *q*-axis EMC model of the investigated LRE-IPMSM is shown in Figure 12 and it is rewritten in Figure 13. To show the *q*-axis EMC model clearly, the structural dimensions of the machine model are adjusted approximately. According to Kirchoff's law, the equations of the *q*-axis magnetic circuit can be obtained as follows:

$$\begin{cases} (R_{g\_q1} + R_{q1})\Phi_{q1} - R_{g\_q2}\Phi_{q2} + F_{S\_q2} - F_{S\_q1} - F_{q1} = 0 \\ R_{g\_q2}\Phi_{q2} + R_{q2}(\Phi_{q1} + \Phi_{q2}) - R_{g\_q3}\Phi_{q3} + F_{S\_q3} - F_{S\_q2} - F_{q2} = 0 \\ R_{g\_q3}\Phi_{q3} + R_{q3}(\Phi_{q1} + \Phi_{q2} + \Phi_{q3}) - F_{S\_q3} - F_{q3} = 0 \end{cases} \quad (10)$$

$$F_{qi} = \frac{F_{Br\_qi}R_{Ba\_qi}}{R_{Ba\_qi} + R_{Br\_qi}} \quad (11)$$

$$R_{qi} = \frac{R_{Br\_qi}R_{Ba\_qi}}{R_{Ba\_qi} + R_{Br\_qi}} \quad (12)$$

where  $R_{g\_qi}$  and  $R_{Ba\_qi}$  are the air gap reluctance and flux barrier reluctance in the *q*-axis magnetic circuit, respectively.  $F_{S\_qi}$  is the MMF produced by the *q*-axis stator current.  $F_{Br\_qi}$  and  $R_{Br\_qi}$  are the equivalent MMF and reluctance of the bridge in the *q*-axis magnetic circuit, respectively.  $\Phi_{qi}$  is the segmental *q*-axis flux that flows through  $R_{g\_qi}$ , as shown in Figure 13.  $F_{qi}$  and  $R_{qi}$  are the equivalent MMF and reluctance of the corresponding flux barrier and bridge parallel circuit, respectively, as shown in Figure 14.

Therefore, the *q*-axis flux ( $\Phi_q$ ) can be expressed as:

$$\Phi_q = \frac{(F_{S\_q1} + F_{q1} - F_{S\_q2})R_{g\_q2}R_{q3} + (F_{S\_q2} + F_{q2} - F_{S\_q3})(R_{g\_q2}R_{g\_q3} + R_{g\_q1}R_{g\_q3} + R_{g\_q3}R_{q1}) + (F_{S\_q3} + F_{q3})R_y}{(R_{g\_q1} + R_{q1})(R_{g\_q2} + R_{q2})(R_{g\_q3} + R_{q3}) + R_{g\_q2}R_{g\_q3}R_{q3} + R_{g\_q3}R_{q3}(R_{g\_q1} + R_{q1}) + R_{g\_q2}R_{q2}(R_{g\_q3} + R_{q3})} \quad (13)$$

$$R_y = R_{g\_q1}R_{g\_q3} + R_{g\_q3}R_{q1} + R_{g\_q1}R_{g\_q2} + R_{g\_q2}R_{q1} + R_{g\_q1}R_{q2} + R_{q1}R_{q2} + R_{g\_q2}R_{q2} + R_{g\_q2}R_{g\_q3} \quad (14)$$

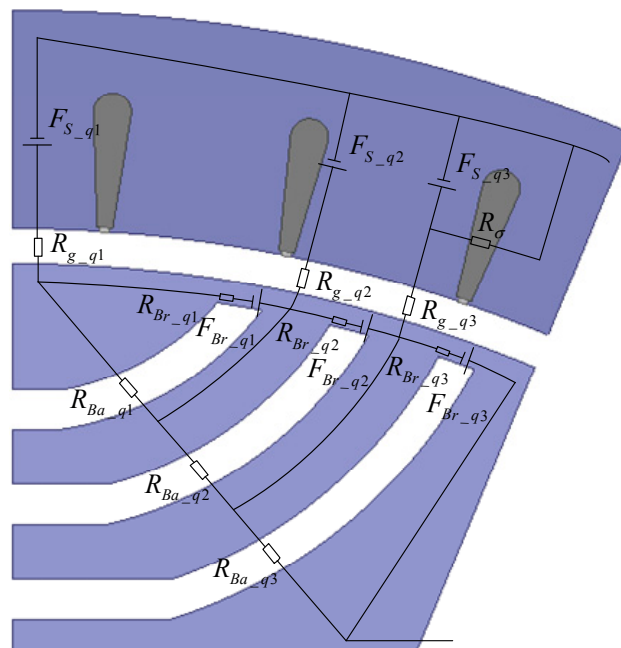


Figure 12. *q*-axis magnetic circuit model.

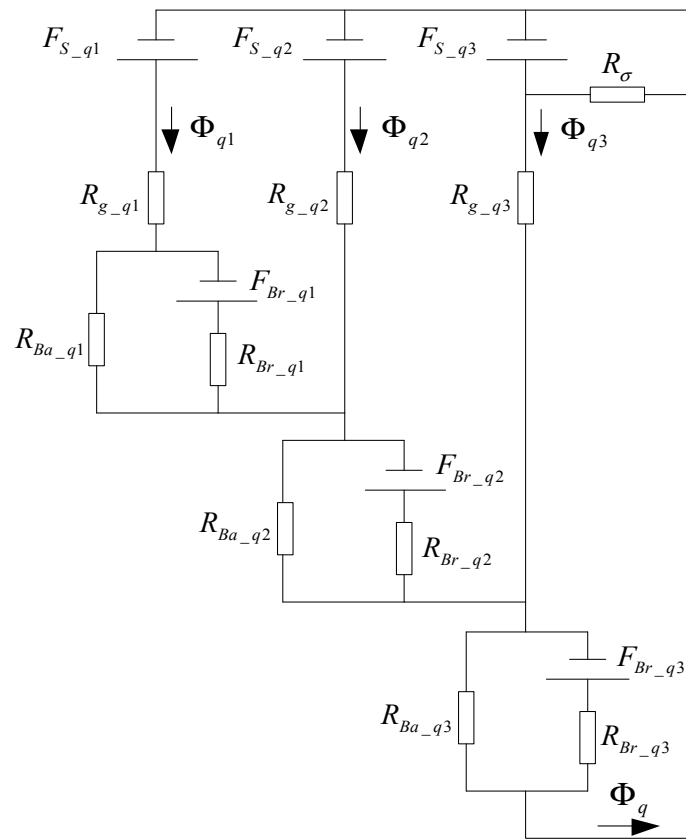


Figure 13. Rewriting of  $q$ -axis magnetic circuit model.

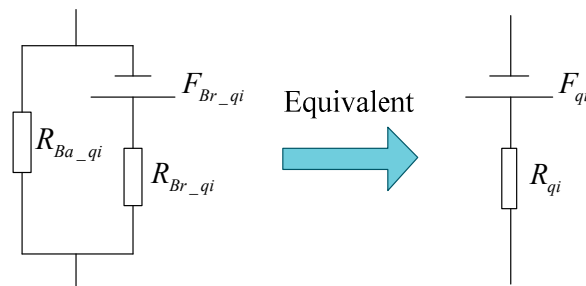


Figure 14. Equivalent of the flux barrier and bridge parallel circuit.

### 3.2. Effect of PM Thickness on $q$ -Axis Flux

When the effects of geometric parameters (including  $h_{PMi}$ ,  $b_{PMi}$ ,  $h_{Bai}$ , and  $\theta_{Bai}$ ) on  $\Phi_q$  are investigated, the bridges are neglected (i.e.,  $b_{Br}=0$ ) to analyze the  $q$ -axis magnetic circuit conveniently. The influence of the bridge width on  $\Phi_q$  is analyzed in the following subsection.

When the  $q$ -axis and  $d$ -axis flux analyses are investigated, the stator current is 371 A. The influence of the PM thickness on  $\Phi_q$  is shown in Figure 15. In the preliminary LRE-IPMSM, the width of the PM in different layers increases in sequence (i.e.,  $b_{PMi} > b_{PMi-1}$ ). A wider PM means that there will be more  $q$ -axis flux flowing through the corresponding PM removed area. Hence the influence of  $h_{PMi}$  on  $\Phi_q$  is more remarkable than  $h_{PMi-1}$ , as shown in Figure 15. In addition, as can be seen in Figure 15,  $\Phi_q$  decreases and the tendency is slowing when  $h_{PMi}$  increases.

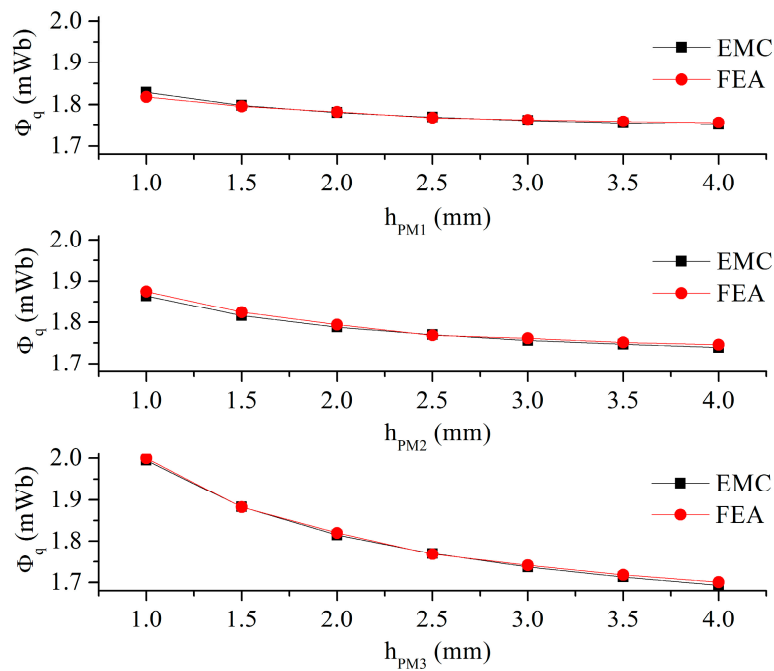


Figure 15.  $q$ -axis flux ( $\Phi_q$ ) versus the PM thickness ( $h_{PMi}$ ).

### 3.3. Effect of PM Width on $q$ -Axis Flux

Figure 16 shows the effect of the PM width on  $\Phi_q$ . For the purpose of analyzing the effect of  $b_{PMi}$  on  $\Phi_q$  simply, the flux barrier thickness is adjusted slightly to keep the reluctance of the flux barrier invariable when  $b_{PMi}$  changes. The reluctance of the PM removed area decreases when the PM width increases, which results in the reduction of  $R_{Ba\_qi}$  as the reluctance of the flux barrier is constant. Hence,  $\Phi_q$  increases with the increment of  $b_{PMi}$ , as shown in Figure 16.

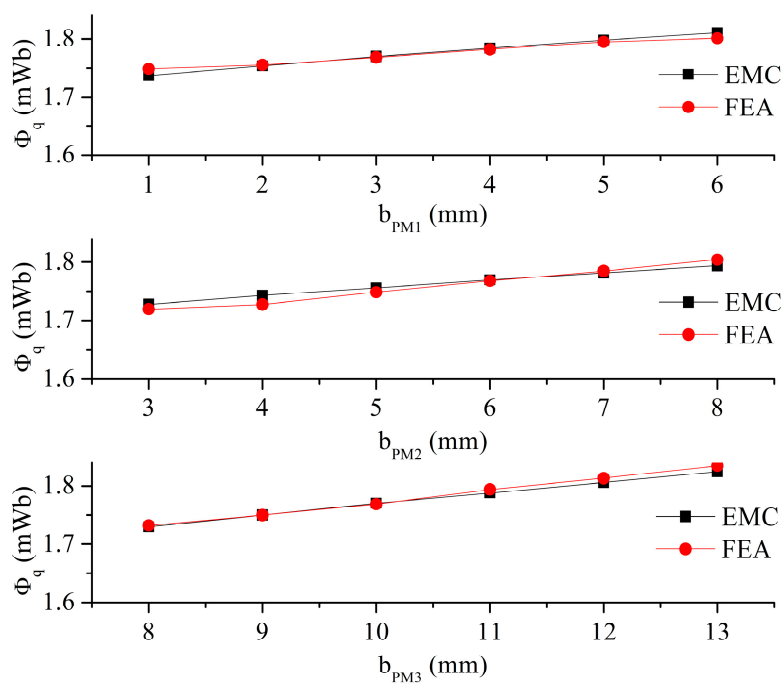


Figure 16.  $q$ -axis flux ( $\Phi_q$ ) versus the PM width ( $b_{PMi}$ ).

### 3.4. Effect of Flux Barrier Thickness on $q$ -Axis Flux

The influence of the flux barrier thickness on  $\Phi_q$  is shown in Figure 17. In the preliminary LRE-IPMSM, the width of the flux barrier in different layers increases in sequence. Hence,  $\Phi_q$  is more sensitive to the variation of  $h_{Ba1}$  than that of  $h_{Ba1-1}$ , as shown in Figure 17. In addition, as can be seen in Figure 17, when  $h_{Ba1}$  increases,  $\Phi_q$  decreases and the tendency is slowing.

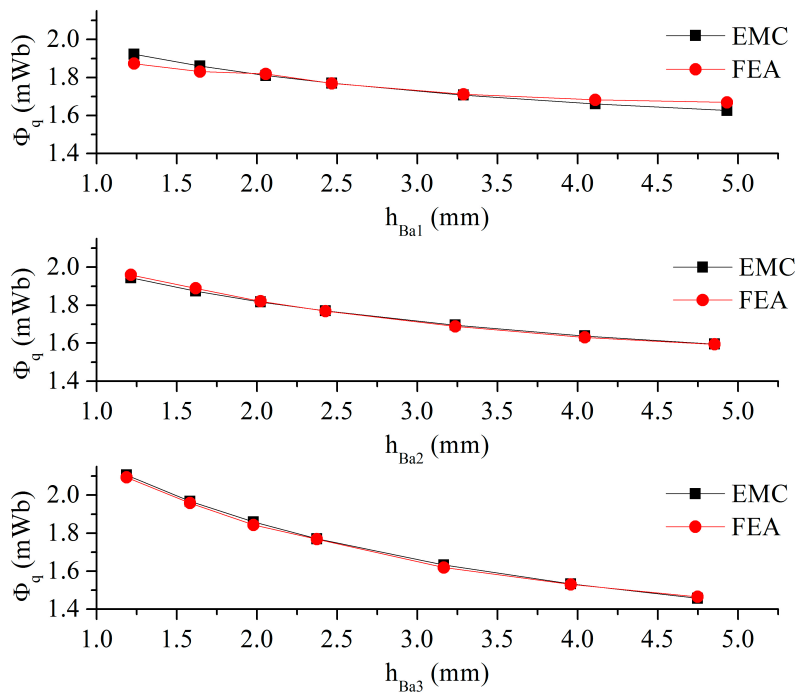


Figure 17.  $q$ -axis flux ( $\Phi_q$ ) versus the flux barrier thickness ( $h_{Ba1}$ ).

### 3.5. Effect of Flux Barrier Span Angle on $q$ -Axis Flux

The effect of the flux barrier span angle on  $\Phi_q$  is shown in Figure 18. When  $\theta_{Ba1}$  increases, there will be more  $q$ -axis flux flowing through the corresponding flux barrier, which means that the  $q$ -axis reluctance increases. Hence,  $\Phi_q$  decreases with the increment of  $\theta_{Ba1}$ , as shown in Figure 18. In addition, it can be seen that when the effect of  $\theta_{Ba1}$  on  $\Phi_q$  is investigated, there is a considerable error between the results of the EMC method and FEA. This is because more  $q$ -axis flux does not flow through the first flux barrier when  $\theta_{Ba1}$  decreases, which results in the saturation of the partial stator teeth and yoke. The saturation area decreases and the error between the results of the EMC method and FEA declines when  $\theta_{Ba1}$  increases, as can be seen in Figure 18. When  $\theta_{Ba2}$  and  $\theta_{Ba3}$  decrease, the stator teeth and yoke are not saturated because the stator MMF  $F_{S\_q2}$  and  $F_{S\_q3}$  are much less than  $F_{S\_q1}$ . Hence, when the effects of  $\theta_{Ba2}$  and  $\theta_{Ba3}$  on  $\Phi_q$  are investigated, the errors between the results of the EMC method and FEA are negligible.

### 3.6. Effect of Bridge Width on $q$ -Axis Flux

Figure 19 shows the variation of  $\Phi_q$  with respect to  $b_{Br}$ . When the bridge width increases, more  $q$ -axis flux flows through the bridges instead of the flux barriers. That results in the increment of  $\Phi_q$  as  $b_{Br}$  increases, as seen in Figure 19. The bridges are saturated all the time when  $b_{Br}$  increases. Therefore, when the variation of  $\Phi_q$  with respect to  $b_{Br}$  is investigated, the error between the results of the EMC method and FEA is negligible.

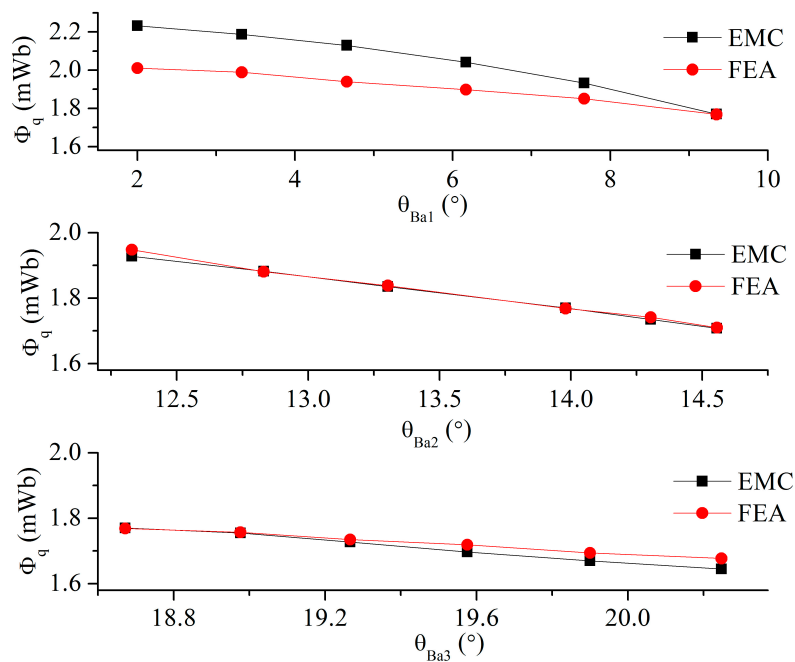


Figure 18.  $q$ -axis flux ( $\Phi_q$ ) versus the flux barrier span angle ( $\theta_{Bai}$ ).

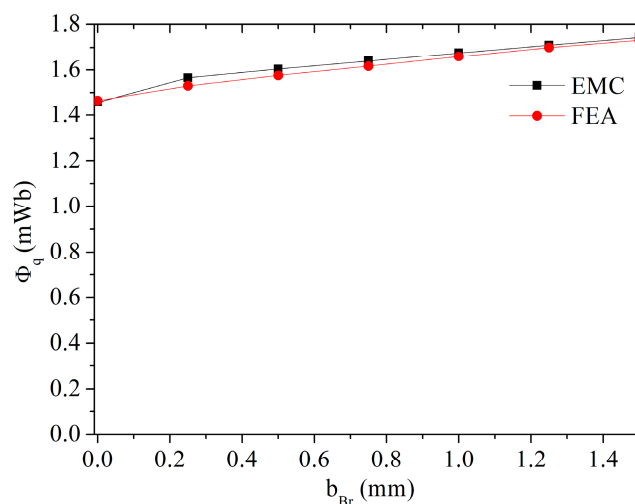


Figure 19.  $q$ -axis flux ( $\Phi_q$ ) versus the bridge width ( $b_{Br}$ ).

## 4. $d$ -Axis Magnetic Circuit Analysis

### 4.1. $d$ -Axis Magnetic Circuit Model

The reluctance of the flux barrier in the  $d$ -axis magnetic circuit is much larger than that of the iron core. Hence, most  $d$ -axis flux above the flux barrier takes the route of the bridge and then the iron core instead of passing through the flux barrier and then the PM removed area, as shown in Figure 20. That results in the flux extrusion and saturation of the iron core at the bridge ends. The saturation area is equivalent to an MMF ( $F_{Br\_di}$ ) and a serial-connected reluctance ( $R_{Br\_di}$ ) in the  $d$ -axis magnetic circuit model.

The reluctance in the  $d$ -axis magnetic circuit is low as the  $d$ -axis flux does not go through the flux barriers. Besides, a large  $d$ -axis current is applied to improve the machine torque density. That results in the saturation of the stator teeth and yoke in the  $d$ -axis magnetic circuit. The stator yoke and teeth are equivalent to the corresponding MMF ( $F_{Sy\_di}$ ,  $F_{St\_di}$ ) and serial-connected reluctance ( $R_{Sy\_di}$ ,  $R_{St\_di}$ ) in

the  $d$ -axis magnetic circuit model, respectively. The  $d$ -axis EMC model of the investigated LRE-IPMSM is shown in Figure 21 and it is rewritten in Figure 22. To show the  $d$ -axis EMC model clearly, the structural dimensions of the machine model are adjusted approximately.

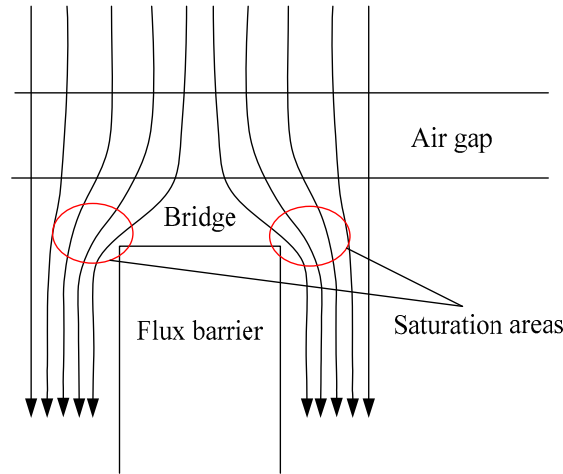


Figure 20. Sketch of  $d$ -axis flux distribution.

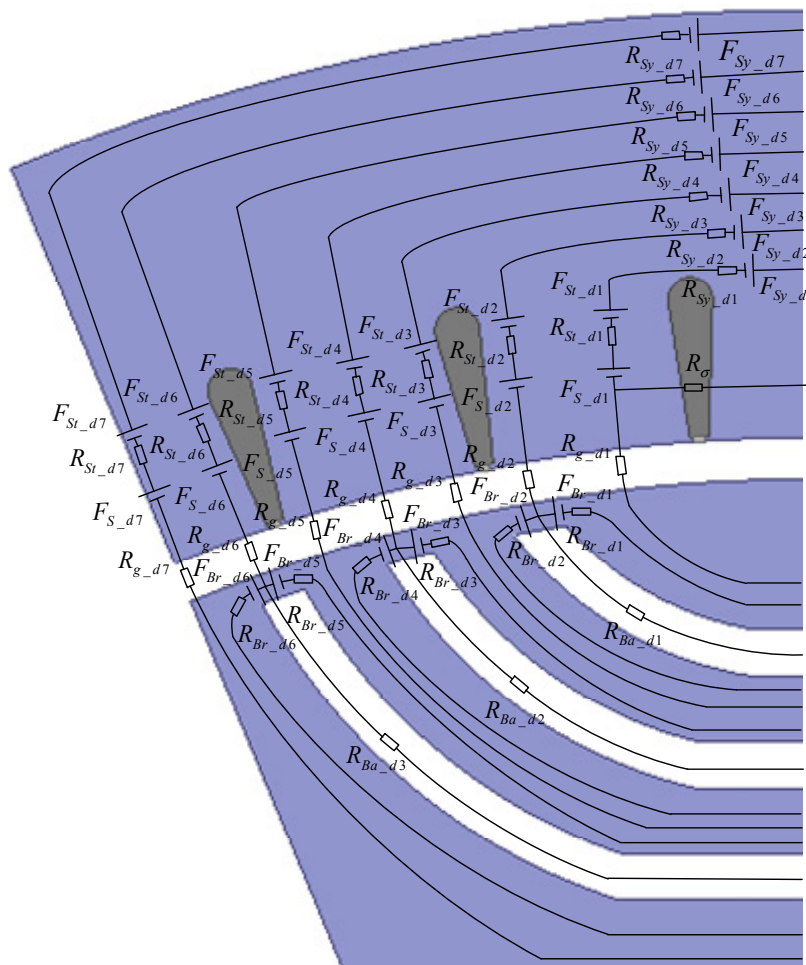


Figure 21.  $d$ -axis magnetic circuit model.

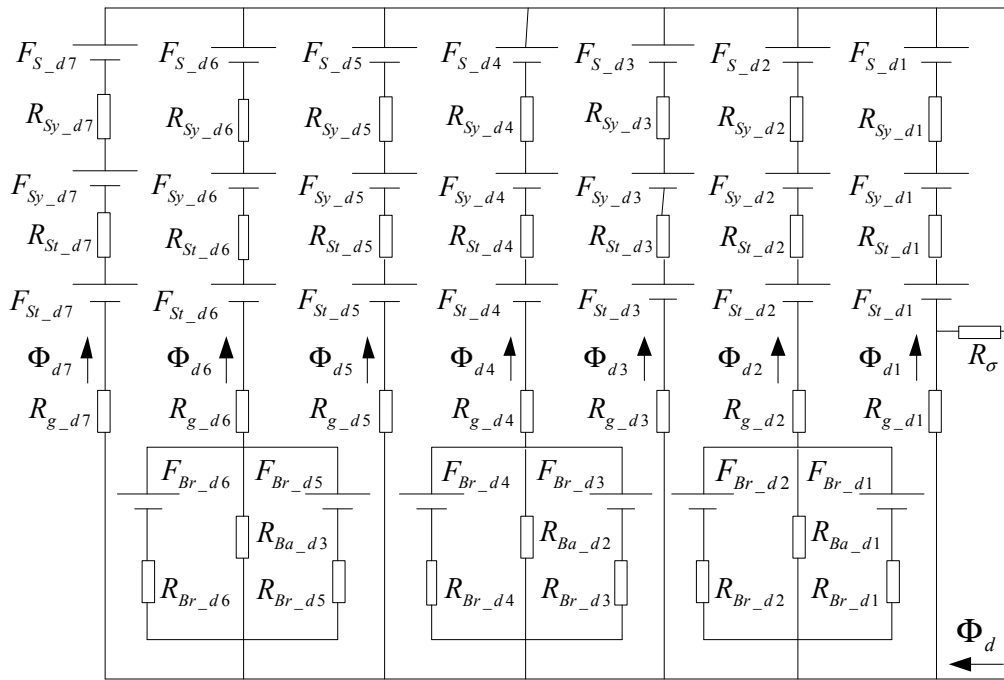


Figure 22. Rewriting of  $d$ -axis magnetic circuit model.

According to Kirchhoff’s law, the  $d$ -axis flux ( $\Phi_d$ ) can be expressed as:

$$\begin{aligned} \Phi_d &= \Phi_{d7} + \Phi_{d6} + \Phi_{d5} + \Phi_{d4} + \Phi_{d3} + \Phi_{d2} + \Phi_{d1} \\ &= \frac{F_{Sy\_d7} + F_{St\_d7} + F_{S\_d7}}{R_{Sy\_d7} + R_{St\_d7} + R_{g\_d7}} + \frac{F_{Sy\_d6} + F_{St\_d6} + F_{S\_d6} + F_{d6}}{R_{Sy\_d6} + R_{St\_d6} + R_{g\_d6} + R_{d6}} + \frac{F_{Sy\_d5} + F_{St\_d5} + F_{S\_d5}}{R_{Sy\_d5} + R_{St\_d5} + R_{g\_d5}} + \frac{F_{Sy\_d4} + F_{St\_d4} + F_{S\_d4} + F_{d4}}{R_{Sy\_d4} + R_{St\_d4} + R_{g\_d4} + R_{d4}} \\ &\quad + \frac{F_{Sy\_d3} + F_{St\_d3} + F_{S\_d3}}{R_{Sy\_d3} + R_{St\_d3} + R_{g\_d3}} + \frac{F_{Sy\_d2} + F_{St\_d2} + F_{S\_d2} + F_{d2}}{R_{Sy\_d2} + R_{St\_d2} + R_{g\_d2} + R_{d2}} + \frac{(F_{Sy\_d1} + F_{St\_d1} + F_{S\_d1}) \frac{R_\sigma}{R_{g\_d1} + R_\sigma}}{R_{Sy\_d1} + R_{St\_d1} + \frac{R_{g\_d1} R_\sigma}{R_{g\_d1} + R_\sigma}} \end{aligned} \quad (15)$$

$$F_{di} = \left( \frac{F_{Br\_d2i}}{R_{Br\_d2i}} + \frac{F_{Br\_d2i-1}}{R_{Br\_d2i-1}} \right) \cdot R_{di} \quad (16)$$

$$\frac{1}{R_{di}} = \frac{1}{R_{Br\_d2i}} + \frac{1}{R_{Br\_d2i-1}} + \frac{1}{R_{Ba\_di}} \quad (17)$$

where  $R_{g\_di}$  and  $R_{Ba\_di}$  are the air gap reluctance and flux barrier reluctance in the  $d$ -axis magnetic circuit, respectively.  $R_\sigma$  is the leakage reluctance.  $F_{S\_di}$  is the MMF produced by the  $d$ -axis stator current.  $\Phi_{di}$  is the segmental  $d$ -axis flux that flows through  $R_{g\_di}$ , as shown in Figure 22.  $F_{di}$  and  $R_{di}$  are the equivalent MMF and reluctance of the corresponding flux barrier and bridges parallel circuit, respectively, as shown in Figure 23.

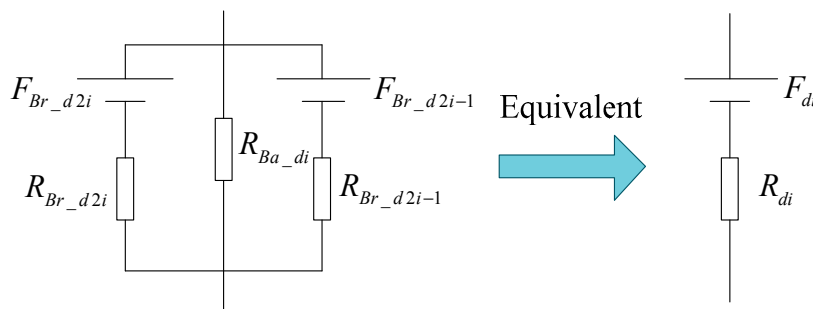


Figure 23. Equivalent of the flux barrier and bridges parallel circuit.

#### 4.2. Effect of PM Thickness on $d$ -Axis Flux

The bridge width affects the saturation area of the bridge end and it is designed to be 0.75 mm preliminarily to study the variations of  $\Phi_d$  with respect to the geometric parameters (including  $h_{PMi}$ ,  $b_{PMi}$ ,  $h_{Bai}$ , and  $\theta_{Bai}$ ). The variation of  $\Phi_d$  with respect to  $h_{PMi}$  is shown in Figure 24. As mentioned before, most  $d$ -axis flux does not flow through the flux barrier and PM removed area. Therefore,  $\Phi_d$  exhibits negligible variation when the PM thickness increases, as shown in Figure 24.

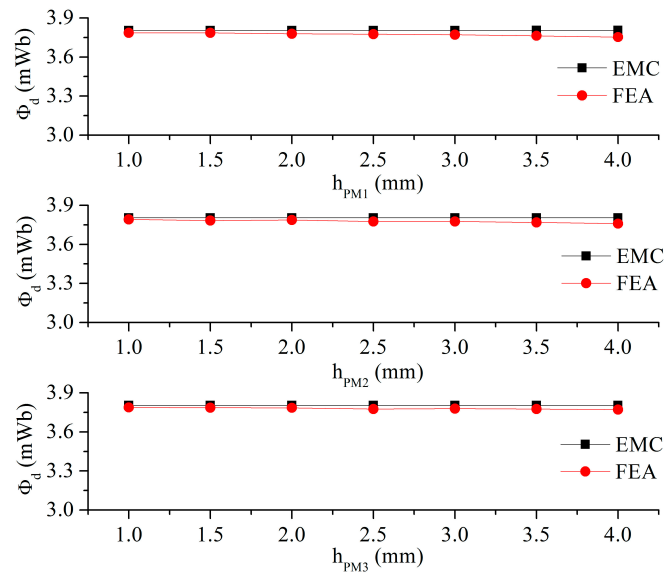


Figure 24.  $d$ -axis flux ( $\Phi_d$ ) versus the PM thickness ( $h_{PMi}$ ).

#### 4.3. Effect of PM Width on $d$ -axis Flux

The variation of  $\Phi_d$  with respect to the PM width is shown in Figure 25. To analyze the effect of  $b_{PMi}$  on  $\Phi_d$  simply, the flux barrier thickness is changed slightly to keep the reluctance of the flux barrier invariable when  $b_{PMi}$  changes. As can be seen,  $\Phi_d$  is almost invariable as the PM width increases, which is the same as the effect of  $h_{PMi}$  on  $\Phi_d$ . This can also be explained by the fact that most  $d$ -axis flux does not flow through the flux barrier and PM removed area.

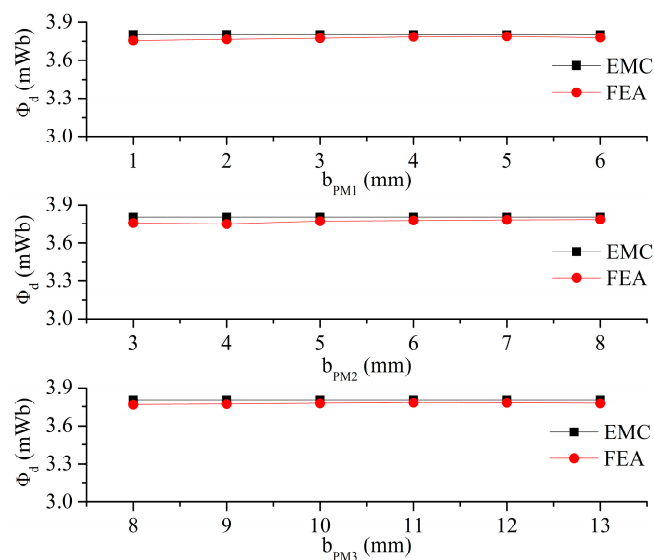


Figure 25.  $d$ -axis flux ( $\Phi_d$ ) versus the PM width ( $b_{PMi}$ ).



#### 4.4. Effect of Flux Barrier Thickness on $d$ -Axis Flux

Figure 26 shows the variation of  $\Phi_d$  with respect to  $h_{Bai}$ . As can be seen,  $\Phi_d$  calculated by FEA decreases as the flux barrier thickness exceeds about 2.5 mm. This is caused by the rotor saturation as  $h_{Bai}$  increases continuously. The rotor saturation is not taken into consideration in the EMC method and hence  $\Phi_d$  calculated by the EMC method is almost invariable. When the PM thickness increases to some extent, it also causes the rotor saturation. However, the saturation area of the rotor is relatively small because the PM width is much less than the flux barrier width in the preliminary LRE-IPMSM. Therefore, when  $h_{PMi}$  increases, the rotor saturation has a negligible impact on  $\Phi_d$ .

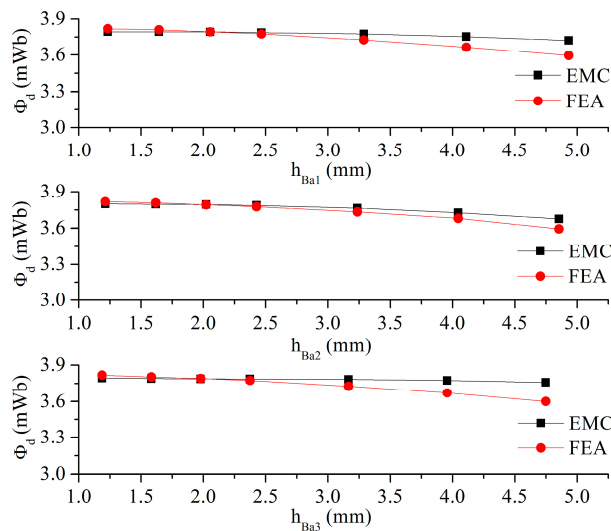


Figure 26.  $d$ -axis flux ( $\Phi_d$ ) versus the flux barrier thickness ( $h_{Bai}$ ).

#### 4.5. Effect of Flux Barrier Span Angle on $d$ -Axis Flux

The effect of  $\theta_{Bai}$  on  $\Phi_d$  is shown in Figure 27. According to the analysis of the  $d$ -axis magnetic circuit, it can be easily known that when the  $i$ -layer flux barrier span angle changes,  $\Phi_{d2i}$ , as well as the sum of  $\Phi_{d2i-1}$  and  $\Phi_{d2i+1}$ , is constant. Besides, the other segmental  $d$ -axis fluxes are scarcely affected by the change of the  $i$ -layer flux barrier span angle. Therefore, the influence of  $\theta_{Bai}$  on  $\Phi_d$  is negligible, as shown in Figure 27.

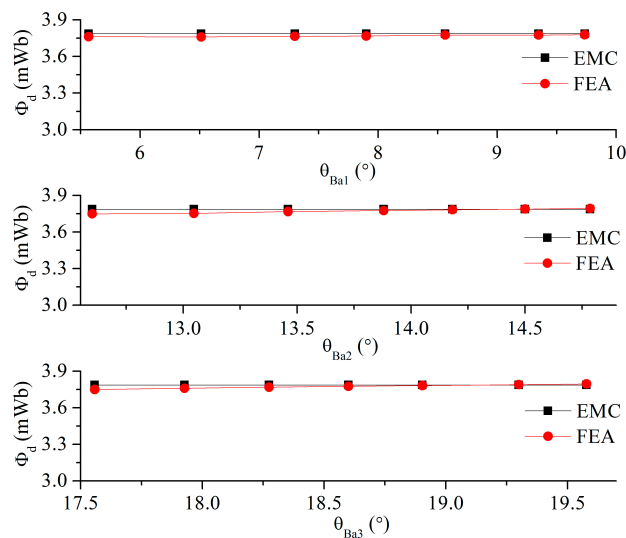
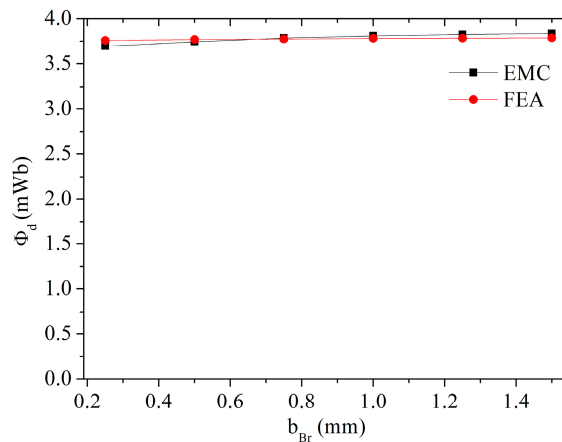


Figure 27.  $d$ -axis flux ( $\Phi_d$ ) versus the flux barrier span angle ( $\theta_{Bai}$ ).

#### 4.6. Effect of Bridge Width on $d$ -Axis Flux

Figure 28 shows the variation of  $\Phi_d$  with respect to  $b_{Br}$ . The saturation level of the bridge end declines as  $b_{Br}$  increases, which inevitably results in the increment of  $\Phi_d$ . However,  $\Phi_d$  increases negligibly, as shown in Figure 28, because the saturation area of the bridge end is far smaller than that of the stator teeth and yoke.



**Figure 28.**  $d$ -axis flux ( $\Phi_d$ ) versus the bridge width ( $b_{Br}$ ).

Besides, as can be seen in Figures 24–28, the result of the EMC method matches well with that of FEA. This is because when the geometric parameters change, the saturation level of the saturation area does not vary obviously due to the small  $d$ -axis reluctance.

### 5. Electromagnetic Performance Analyses

In the previous sections, the no-load,  $q$ -axis, and  $d$ -axis magnetic circuits of the LRE-IPMSM are studied. The EMC method, which costs less time than FEA, is an effective tool in the preliminary design procedure of the LRE-IPMSMs. Additionally, the structure design of the LRE-IPMSMs can be refined by the results of FEA as the FEA provides more accurate and detailed results compared with the EMC method. Figure 29 shows an optimized design of the LRE-IPMSM, which is obtained by the analyses of the EMC method and FEA after weighing various electromagnetic and mechanical performances. The bridge width is designed to be 1.5 mm with the electromagnetic performances and mechanical strength taken into consideration. The electromagnetic performances of the optimized LRE-IPMSM are studied in this section.

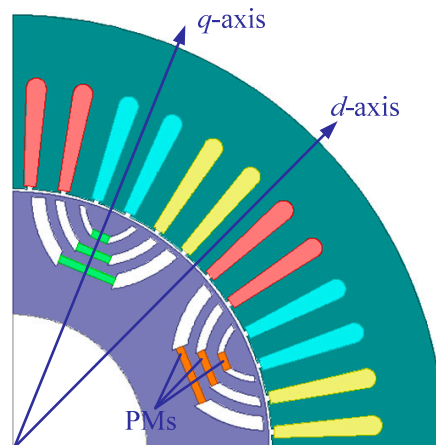


**Figure 29.** Sketch of the optimized LRE-IPMSM.

### 5.1. Torque Characteristics

When the optimized LRE-IPMSM is controlled by the maximum torque-per-ampere (MTPA) and the stator current is 371 A, the PM torque, reluctance torque, and electromagnetic torque calculated by the EMC method and FEA are shown in Figure 30. As shown in Figure 30, there is an error between the results of the EMC method and FEA. The error of the PM torque is mainly caused by the decline of the bridge saturation level as the bridge width is selected to be 1.5 mm by taking the mechanical strength into consideration. The error of the reluctance torque is mainly caused by the cross coupling effect. The electromagnetic torque is 361.69 Nm (FEA), which is larger than the target torque of 344 Nm. The reluctance torque is 257 Nm (FEA), which accounts for 71% of the electromagnetic torque at this operating point.

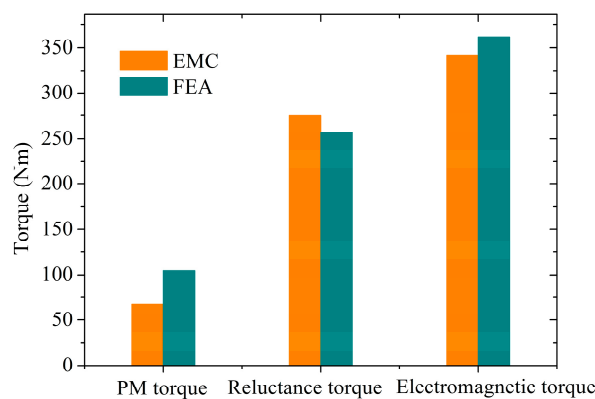


Figure 30. Various torques calculated by the EMC method and FEA.

When the electromagnetic torque reaches the maximum, the waveforms of the electromagnetic torque and reluctance torque calculated by FEA are shown in Figure 31. As shown in Figure 31, the torque ripples of the electromagnetic torque and reluctance torque are 5.39% and 4.74%, respectively. The results illustrate that the optimized LRE-IPMSM owns the merit of low torque ripple, which is crucial to the comfort of the EVs.

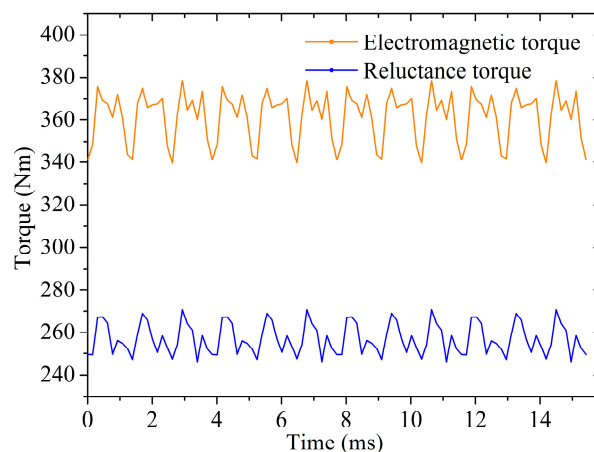


Figure 31. Waveforms of electromagnetic torque and reluctance torque.

### 5.2. Loss and Efficiency Characteristics

Figure 32 shows the loss and efficiency over the whole speed range. As shown in Figure 32, the copper loss is constant below 3500 rpm as the current is constant under MTPA control and it decreases beyond 3500 rpm as the current drops under the maximum torque-per-voltage (MTPV)

control. The stator and rotor iron losses increase significantly with the increment of speed. The efficiency reaches the maximum of 96.4% at 6500 rpm, which exceeds the target efficiency of 96%.

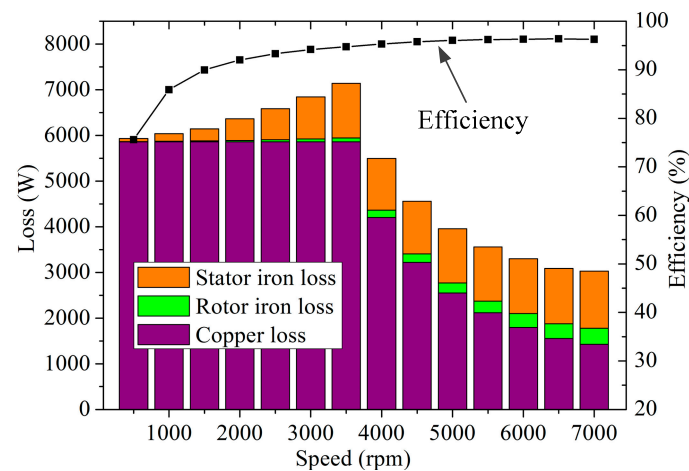


Figure 32. Loss and efficiency over the whole speed range.

## 6. Mechanical Strength Verification

When the optimized LRE-IPMSM works at the maximum speed, the stress distribution of the optimized LRE-IPMSM is shown in Figure 33. According to the structure analysis of rotor, it can be found that the third bridge is the stress concentration in the rotor. Hence, the maximum stress occurs in the third bridge and its value is 274.63 MPa, as shown in Figure 33. The yield strength of the silicon steel is about 330 MPa, and therefore, the optimized LRE-IPMSM satisfies the requirement of mechanical strength.

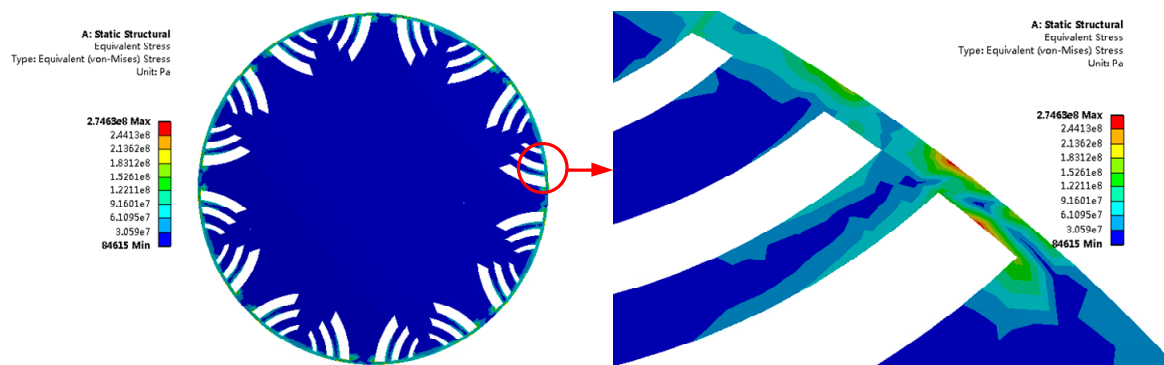


Figure 33. Stress distribution at maximum speed.

## 7. Conclusions

The following conclusions can be drawn from the magnetic circuit and performance analyses of LRE-IPMSM:

- (1) The PM width has a significant influence on the no-load flux, but the PM thickness does not. Thickening the third flux barrier and increasing the third flux barrier span angle can increase the no-load flux.
- (2) Thickening the PM and flux barrier, as well as increasing the flux barrier span angle, can decrease the  $q$ -axis flux, while widening the PM increases the  $q$ -axis flux.

- (3) The PM width and PM thickness, as well as the flux barrier span angle, affect the  $d$ -axis flux negligibly. The rotor saturation results in  $d$ -axis flux reduction as the flux barrier thickness increases continuously.
- (4) Widening the bridge can decrease the no-load flux and increase the  $q$ -axis flux obviously. However, the bridge width affects the  $d$ -axis flux negligibly because the saturation area of the bridge end is far smaller than that of the stator teeth and yoke.
- (5) The analyses of the EMC models can be extended to the rotor structure with a different number of poles and different layers of the flux barriers, as well as various types of materials. However, when the stator current changes, the accuracy of EMC models declines (especially in the  $d$ -axis model) because of the variation of the saturation level. Hence, the accuracy of torque calculation by the EMC method declines as the stator current changes.
- (6) It is shown by the electromagnetic performance of the optimized LRE-IPMSM that the electromagnetic torque reaches 361.69 Nm and the electromagnetic torque ripple is 5.39% under MTPA control of 371 A. The efficiency reaches the maximum of 96.4% at 6500 rpm. The stress distribution of the optimized LRE-IPMSM at maximum speed is obtained. The result shows that the optimized LRE-IPMSM satisfies the requirement of mechanical strength.

**Acknowledgments:** This work was supported in part by National Key R&D Program of China under Project 2017YFB0203603, in part by National Natural Science Foundation of China under Project 51325701, 51637003 and 51521003, in part by Self-Planned Task (No. 201504B) of State Key Laboratory of Robotics and System (HIT), and in part by the Fundamental Research Funds for the Central Universities (Grant No. HIT.MKSTISP.2016 24).

**Author Contributions:** The work presented here was carried out through the cooperation of all authors. Ping Zheng and Weinan Wang conducted the research and wrote the paper. Mingqiao Wang edited the manuscript including the literature review. Yong Liu supervised the whole study. Zhenxing Fu provided feedback for improvement of the original manuscript. All authors read and approved the manuscript.

**Conflicts of Interest:** The authors declare no conflict of interest.

## References

1. Boldea, I.; Tutelea, L.; Parsa, L.; Dorrell, D. Automotive electric propulsion systems with reduced or no permanent magnets: An overview. *IEEE Trans. Ind. Electron.* **2014**, *61*, 5696–5711. [[CrossRef](#)]
2. Degano, M.; Carraro, E.; Bianchi, N. Selection criteria and robust optimization of a traction PM-assisted synchronous reluctance motor. *IEEE Trans. Ind. Appl.* **2015**, *51*, 4383–4391. [[CrossRef](#)]
3. Vagati, A.; Boazzo, B.; Guglielmi, P.; Pellegrino, G. Design of ferrite-assisted synchronous reluctance machines robust toward demagnetization. *IEEE Trans. Ind. Appl.* **2014**, *50*, 1768–1779. [[CrossRef](#)]
4. Morimoto, S.; Ooi, S.; Inoue, Y.; Sanada, M. Experimental evaluation of a rare-earth-free PMASynRM with ferrite magnets for automotive applications. *IEEE Trans. Ind. Electron.* **2014**, *61*, 5749–5756. [[CrossRef](#)]
5. Boazzo, B.; Vagati, A.; Pellegrino, G.; Armando, E.; Guglielmi, P. Multipolar ferrite-assisted synchronous reluctance machines: A general design approach. *IEEE Trans. Ind. Electron.* **2015**, *62*, 832–845. [[CrossRef](#)]
6. Lazari, P.; Wang, J.; Sen, B. 3-D effects of rotor step-skews in permanent magnet-assisted synchronous reluctance machines. *IEEE Trans. Magn.* **2015**, *51*, 8112704. [[CrossRef](#)]
7. Wang, Y.; Ionel, D.M.; Jiang, M.; Stretz, S.J. Establishing the relative merits of synchronous reluctance and PM-assisted technology through systematic design optimization. *IEEE Trans. Ind. Appl.* **2016**, *52*, 2971–2978. [[CrossRef](#)]
8. Bianchi, N.; Fornasiero, E.; Ferrari, M.; Castiello, M. Experimental comparison of PM-assisted synchronous reluctance motors. *IEEE Trans. Ind. Appl.* **2016**, *52*, 163–171. [[CrossRef](#)]
9. Carraro, E.; Morandin, M.; Bianchi, N. Traction PMASR motor optimization according to a given driving cycle. *IEEE Trans. Ind. Appl.* **2016**, *52*, 209–216. [[CrossRef](#)]
10. Bianchi, N.; Bolognani, S.; Bon, D.; Pr e, M.D. Rotor flux-barrier design for torque ripple reduction in synchronous reluctance and PM-assisted synchronous reluctance motors. *IEEE Trans. Ind. Appl.* **2009**, *45*, 921–928. [[CrossRef](#)]

11. Obata, M.; Morimoto, S.; Sanada, M.; Inoue, Y. Performance evaluation of high power and low torque ripple structure of rare-earth free PMASynRM with ferrite magnet. In Proceedings of the 10th IEEE International Conference on Power Electronics and Drive Systems (PEDS), Kitakyushu, Japan, 22–25 April 2013; pp. 714–719.
12. Ooi, S.; Morimoto, S.; Sanada, M.; Inoue, Y. Performance evaluation of a high-power-density PMASynRM with ferrite magnets. *IEEE Trans. Ind. Appl.* **2013**, *49*, 1308–1315. [[CrossRef](#)]
13. Carraro, E.; Degano, M.; Bianchi, N. Permanent magnet volume minimization in permanent magnet assisted synchronous reluctance motors. In Proceedings of the 8th International Conference and Exhibition on Ecological Vehicles and Renewable Energies (EVER), Monte Carlo, Monaco, 27–30 March 2013; pp. 1–4.
14. Guglielmi, P.; Boazzo, B.; Armando, E.; Pellegrino, G.; Vagati, A. Permanent-magnet minimization in PM-assisted synchronous reluctance motors for wide speed range. *IEEE Trans. Ind. Appl.* **2013**, *49*, 31–41. [[CrossRef](#)]
15. Calvo, E.S.; Potoradi, D. Synchronous reluctance motors with and without permanent magnets for high performance low cost electrical drives. In Proceedings of the 5th International Electric Drives Production Conference (EDPC), Nuremberg, Germany, 15–16 September 2015; pp. 1–7.
16. Zhu, L.; Jiang, S.Z.; Zhu, Z.Q.; Chan, C.C. Analytical modeling of open-circuit air-gap field distributions in multisegment and multilayer interior permanent-magnet machines. *IEEE Trans. Magn.* **2009**, *45*, 3121–3130. [[CrossRef](#)]
17. Bianchi, N.; Mahmoud, H. An analytical approach to design the PM in PMAREL motors robust toward the demagnetization. *IEEE Trans. Energy Convers.* **2016**, *31*, 800–809. [[CrossRef](#)]



© 2017 by the authors. Licensee MDPI, Basel, Switzerland. This article is an open access article distributed under the terms and conditions of the Creative Commons Attribution (CC BY) license (<http://creativecommons.org/licenses/by/4.0/>).